Journal of Biomedical Optics

BiomedicalOptics.SPIEDigitalLibrary.org

Super-resolution photoacoustic microscopy using photonic nanojets: a simulation study

Paul Kumar Upputuri
Zhuo-Bin Wen
Zhe Wu
Manojit Pramanik

SPIE.

Super-resolution photoacoustic microscopy using photonic nanojets: a simulation study

Paul Kumar Upputuri,[a] Zhuo-Bin Wen,[b] Zhe Wu,[b] and Manojit Pramanik[a,*]
[a]Nanyang Technological University, School of Chemical and Biomedical Engineering, Biomedical Imaging Laboratory, 70 Nanyang Drive, Singapore 637457, Singapore
[b]University of Electronic Science and Technology of China, School of Physical Electronics, National Laboratory for Vacuum Electronics, Chengdu 610054, China

Abstract. Optical resolution photoacoustic microscopy (ORPAM) is important for various biomedical applications, such as the study of cellular structures, microcirculation systems, and tumor angiogenesis. However, the lateral resolution of a conventional ORPAM is limited by optical diffraction. In this work, we report a simulation study to achieve subdiffraction-limited super-resolution in ORPAM using microspheres. Laser radiation is focused through a microsphere to generate a photonic nanojet, which provides the possibility to break the diffraction limit in ORPAM by reducing the size of the excitation volume. In our simulations using microspheres, we observed improvement in the lateral resolution up to ~fourfold compared to conventional ORPAM. The method is simple, cost effective, and can provide far-field resolution. This approach may provide new opportunities for many biomedical imaging applications that require finer resolution. © *2014 Society of Photo-Optical Instrumentation Engineers (SPIE)* [DOI: 10.1117/1.JBO.19.11.116003]

Keywords: photoacoustic microscopy; super-resolution; subdiffraction-limited imaging; photonic nanojet.

Paper 140514R received Aug. 11, 2014; revised manuscript received Sep. 30, 2014; accepted for publication Oct. 6, 2014; published online Nov. 3, 2014.

1 Introduction

Photoacoustic imaging (PAI) is a rapidly emerging hybrid biomedical imaging modality to study organelles to organs.[1–3] PAI combines the advantage of rich optical contrast and high ultrasonic resolution at depth. In PAI, a short-pulsed laser source irradiates the tissue. Due to absorption of incident energy by the tissue, there is a local temperature rise, which in turn produces pressure waves emitted in the form of acoustic waves, known as photoacoustic (PA) waves. In photoacoustic tomography (PAT), nonfocused wideband ultrasound detectors noninvasively (placed around the target object) acquire the PA waves generated from the tissue.[4–7] Reconstruction techniques are used to map the initial pressure rise within the tissue from the measured PA waves.[8–12] Initial pressure is in turn related to the absorption coefficient of the tissue.

In photoacoustic microscopy (PAM), typically a focused ultrasound transducer or a focused light source (or both in a confocal geometry) is used and depth-resolved PA signals are recorded [similar to the one-dimensional acoustic signals or A-lines in pulse-echo ultrasound imaging]. Then, a raster scan is done to form a two-dimensional (2-D) or three-dimensional map of optical absorption inside the tissue without the use of any explicit reconstruction algorithms.[13] Depending on whether the ultrasound detector or excitation light focus is finer, PAM is classified into acoustic-resolution PAM (ARPAM)[14,15] and optical-resolution PAM (ORPAM).[16–20] The ARPAM, where the detector focus is finer, has achieved a lateral resolution of 45 μm and an imaging depth of 3 mm with 50 MHz, 0.44-NA ultrasound transducer.[15] The ORPAM, where the optical focus is finer, offers optical diffraction-limited lateral resolution which can be as small as micrometers or sub micrometers. In both ORPAM and ARPAM, the axial resolution is limited by the detector bandwidth (typically 50, 75, 125 MHz).[21,22] In this work, we will be discussing only the lateral resolution of ORPAM. The penetration depth of ORPAM is slightly higher than or comparable to the existing optical modalities, such as optical, fluorescence, two-photon microscopy, and optical coherence tomography. However, ORPAM is sensitive to optical absorption with a relative sensitivity of 100% due to background-free detection, whereas the other modalities are sensitive to fluorescence or optical scattering.[23,24]

The optical-diffraction–limited lateral resolution in ORPAM is given by $R_o = 0.51\lambda/\mathrm{NA}$, where λ denotes the optical wavelength and NA is the numerical aperture of the optical objective.[3] Since R_o mainly depends on optical focus, a straight forward method for improving it is to increase the NA. However, the shortcomings of the high-NA objectives (very expensive and short working distances) reduce the flexibility of the system for *in vivo* imaging. A 220 nm ($\sim\lambda/2$) subwavelength (yet diffraction limited) resolution was achieved by using a water-immersion optical objective with NA = 1.23 and $\lambda = 532$ nm.[16] Thus, in ORPAM, the optical focal spot is the key for controlling the lateral resolution—the tighter the optical focus, the finer the image resolution.

Several recent publications have shown that microspheres could be a relatively simple way of achieving far-field super-resolution in optical microscopy.[25–29] A resolution of 50 nm was achieved using fused silica microspheres.[26] When a microsphere is illuminated by a light beam, a subdiffraction photonic nanojet is generated on the shadow side of the microsphere. The existence of such a nanojet provides the possibility of breaking the diffraction limit in optical microscopy by greatly reducing the size of the excitation volume, and the signal generated in the

*Address all correspondence to: Manojit Pramanik, E-mail: manojit@ntu.edu.sg

0091-3286/2014/$25.00 © 2014 SPIE

excitation volume can still be collected in the far-field. Using photonic nanojets, super-resolution imaging was successfully demonstrated in optical microscopy,[26–28] fluorescence microscopy,[30] Raman microscopy,[31] and coherent anti-stokes Raman scattering microscopy.[32] Not much work has been reported on super-resolution ORPAM imaging until now. Using a double-excitation process, subdiffraction-limited lateral resolution was recently demonstrated in photoimprint PAM.[33] A blind-deconvolution optical-resolution photoacoustic microscopy (BD-PAM) that can provide a lateral resolution ~twofold finer than that of conventional OR-PAM is demonstrated.[34] No work has been reported until now on the use of photonic nanojets for super-resolution ORPAM imaging. This approach is simple, cost effective, and can provide far-field super-resolution.

In this work, the possibility to achieve super-resolution in a water medium using microspheres was first investigated. In COMSOL, Gaussian foci were generated using ideal optical objectives with numerical apertures NA = 1.0, 0.7, 0.5 (typically used in ORPAM) in a water medium for different incident wavelengths $\lambda_1 = 532$ nm, $\lambda_2 = 850$ nm, and $\lambda_3 = 1064$ nm. Then photonic nanojets were generated by focusing the Gaussian beams through the dielectric microspheres with diameters of (D) 5, 10, and 15 μm. The materials used for the microsphere are $n_2 = 1.46$ (fused silica), 1.6 (polystyrene), and 2.20 (TiO2–BaO–ZnO glass) and they are embedded in media with a refractive index of $n_1 = 1.33$ (water). The fluence maps generated from COMSOL for Gaussian foci and photonic nanojets were used in a PAM simulation study using the k-wave MATLAB toolbox.[35] Super-resolution in ORPAM using microspheres was achieved. In this simulation study, ~fourfold enhancement in the lateral resolution compared to conventional ORPAM was observed.

2 Methods

In this work, COMSOL Multiphysics software version 4.2a was used for simulating the Gaussian foci and photonic nanojets in a water medium. A desktop with an Intel xeon 3.4 GHz 64-bit processor, 16-GB RAM with a Windows operating system was used for all the COMSOL simulations done in this study. The fluence maps generated from COMSOL were then used in MATLAB for k-wave simulation. The k-wave toolbox,[36] an open source MATLAB toolbox, was used to generate the simulated PA microscopic data. The k-wave toolbox was used only to simulate the PA data generation; no reconstruction technique was used for image formation. A desktop computer with an Intel i5, 2.8 GHz 32-bit processor, 4-GB RAM with a Windows operating system was used for all the k-wave simulations in this study.

2.1 *Simulation of Gaussian Foci/Photonic Nanojets in COMSOL*

COMSOL Multiphysics software works based on the finite element method (FEM) for various physics and engineering applications. Based on electromagnetic theory, a 2-D FEM simulation was designed. The simulation model is illustrated in Fig. 1(a). With scattering boundary conditions (black lines), simulations were carried out in a rectangular area (30×60 μm^2), which includes a water region and a microsphere region. The medium blue region is water, defined by a refractive index $n_1 = 1.33$. A dielectric microsphere (green region) defined by a refractive index (n_2) was embedded in water. The materials used for microspheres in the simulation are fused silica ($n_2 = 1.46$), polystyrene ($n_2 = 1.60$), and TiO2–BaO–ZnO glass ($n_2 = 2.20$). We simulated a focusing laser beam by a TM Gaussian beam propagating along the $+y$-axis with a full width at half maximum (FWHM) beam waist diameter of ($\lambda/2$NA) or an e^{-2} radius of ($\lambda/2.35$NA) in intensity,[32] where λ (532, 850, or 1064 nm) is incident wavelength, and NA (0.5, 0.7, or 1.0) is the numerical aperture of the objective. The beam waist was always centered laterally in the simulation area ($x = 0$), but the y-position varied for different simulations. In the model settings, a smaller mesh element (20 nm) was specified in the Gaussian focus/photonic nanojet region. Outside this region, a larger mesh element (200 nm) was used. The computational time for calculating a 30×60-μm^2 surface plot was 9 s. Several simulations were carried out by changing the diameter of the microsphere (D), the incident wavelength (λ), the numerical aperture of the objective (NA), and the refractive index of the microsphere (n_2). Table 1 summarizes the FWHM values of the Gaussian foci and nanojets for various cases. Table 1 is discussed in detail in Sec. 3.1.

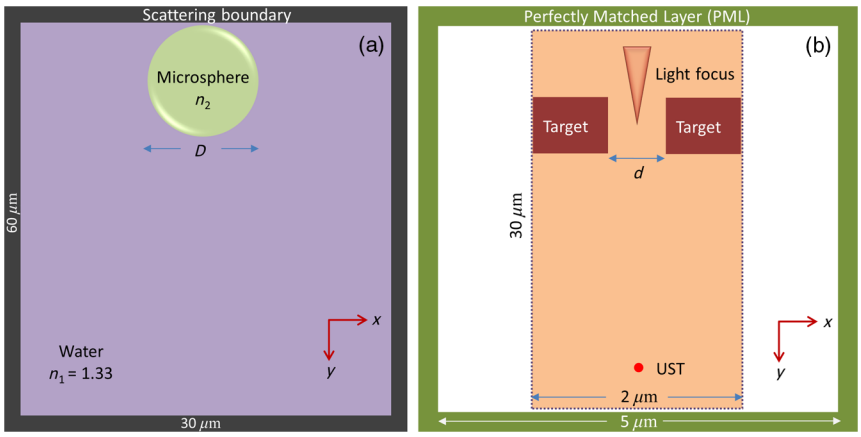

Fig. 1 Schematic diagram of the two-dimensional simulation geometry for (a) photonic nanojet generation using finite element method (FEM) in COMSOL, and (b) photoacoustic microscopy imaging using k-wave toolbox in MATLAB. Here, n_1 and n_2 are the refractive indices of water and microsphere, respectively. UST: ultrasound transducer (point detector). D: diameter of the microsphere. d: distance between the targets.

Table 1 Full width half maximum (FWHM) of Gaussian focus (fg) and photonic nanojet (fp) for different incident wavelengths (λ) in water ($n_1 = 1.33$). (a) $D = 5$ μm, NA = 1.0; (b) $D = 10$ μm, NA = 0.7; (c) $D = 15$ μm, NA = 0.5. Here, D: diameter of the microsphere, n_2: refractive index of micropsphere, NA: numerical aperture of the light focusing lens. Both the FWHM values and the FWHM divided by the incident wavelength (λ) are given in the table. The symbol 'X' in indicates that a nanojet was not observed in these cases.

		$\lambda_1 = 532$ nm			$\lambda_2 = 850$ nm			$\lambda_3 = 1064$ nm		
NA	n_2	fg	fp	fg/fp	fg	fp	fg/fp	fg	fp	fg/fp
(a) $D = 5$ μm										
1.0	1.46	$0.64\lambda_1$ (343 nm)	$0.50\lambda_1$ (266 nm)	1.28	$0.59\lambda_2$ (499 nm)	$0.44\lambda_2$ (375 nm)	1.34	$0.68\lambda_3$ (724 nm)	$0.44\lambda_3$ (464 nm)	1.55
	1.60		$0.39\lambda_1$ (208 nm)	1.64		$0.36\lambda_2$ (309 nm)	1.64		$0.33\lambda_3$ (350 nm)	2.06
	2.20		X	X		$0.33\lambda_2$ (281 nm)	1.79		$0.31\lambda_3$ (327 nm)	2.19
(b) $D = 10$ μm										
0.7	1.46	$0.83\lambda_1$ (441 nm)	$0.64\lambda_1$ (348 nm)	1.30	$0.78\lambda_2$ (662 nm)	$0.62\lambda_2$ (525 nm)	1.26	$0.77\lambda_3$ (821 nm)	$0.60\lambda_3$ (640 nm)	1.28
	1.60		$0.52\lambda_1$ (274 nm)	1.60		$0.61\lambda_2$ (522 nm)	1.28		$0.45\lambda_3$ (481 nm)	1.71
	2.20		X	X		$0.35\lambda_2$ (300 nm)	2.23		$0.29\lambda_3$ (312 nm)	2.66
(c) $D = 15$ μm										
0.5	1.46	$1.05\lambda_1$ (556 nm)	$0.82\lambda_1$ (437 nm)	1.28	$1.03\lambda_2$ (876 nm)	$0.80\lambda_2$ (684 nm)	1.29	$1.09\lambda_3$ (1164 nm)	$0.87\lambda_3$ (928 nm)	1.17
	1.60		$0.65\lambda_1$ (345 nm)	1.62		$0.66\lambda_2$ (559 nm)	1.56		$0.71\lambda_3$ (756 nm)	1.44
	2.20		X	X		$0.39\lambda_2$ (335 nm)	2.64		$0.29\lambda_3$ (305 nm)	3.82

2.2 *Simulation of Photoacoustic Microscopic B-Scan Images using k-Wave Toolbox in MATLAB*

Figure 1(b) shows the simulation geometry used for the simulation of B-scan ORPAM images' acquisition. For simplicity, all simulations were done in 2-D without losing any generality. A computational grid of 251×1501 pixels (the white region of size 5×30 μm, 20 nm/pixel) was used. A perfectly matched boundary layer to satisfy the boundary condition was used for the generation of the forward PA data. A point detector (the red dot) was used for the simulations and was placed at a distance of 26 μm from the target center. The center frequency and the bandwidth of the detector were taken as 125 MHz and 70%, respectively. The transducer parameters are chosen to match the transducers typically used in an ORPAM system,[37] however, instead of a large focusing transducer, a point detector was used to simplify the simulations. Other transducers with lower or higher center frequencies (and bandwidths) can also be used in the simulation. The axial resolution in PAM is related to the bandwidth of the ultrasound transducer and will not affect the lateral resolution of the imaging system. The lateral resolution is primarily determined by the focusing of light in the ORPAM imaging system.

The scanning region was restricted to 101×1501 pixels (the orange region of size 2×30 μm^2). For forward PA simulation, the time step chosen was 0.05 ns with a total of 600 time steps. The simulations assumed a sound speed of 1500 m/s in the medium. For simplicity, the medium was considered acoustically homogeneous and there was no absorption or dispersion of sound. From the simulated pressure waves, PA waves were down sampled five times to mimic a data acquisition system with 4 GigaSamples/s. In all the cases, 1% noise was added with the data, resulting in a 40-dB signal-to-noise ratio. The PAM scan head (in simulation the light source and the detector pair) was moved along the x-direction with a step size of 20 nm, resulting in a total of 101 A-lines per B-scan. The A-line data were stacked after taking Hilbert transform to form a B-scan PAM image. The computational time for each A-line was 2 min 10 s.

Three numerical phantoms were used for the study. The first phantom was a line target with a 0.02-μm width along x-axis and a 1-μm length along y-axis (width $\ll$ expected lateral resolution of the imaging system, making it a line target). This was used as a line object to measure the point spread function along the lateral direction. The second object consisted of two square targets with a side length 1 μm separated by a distance (d) of 0.5 μm. The third one consisted of two square targets with a side length 1 μm separated by a distance (d) of 0.2 μm. In all the phantoms, the targets were binary, therefore, outside the targets there was no initial pressure rise and inside the target the initial pressure rise was 1.

3 Results and Discussion

3.1 *Gaussian Foci and Photonic Nanojets in Water Medium*

As discussed in Sec. 2.1, simulations for the incident wavelengths ($\lambda_1 = 532$ nm, $\lambda_2 = 850$ nm, and $\lambda_3 = 1064$ nm), sphere diameters ($D = 5$, 10, 15 μm), and numerical apertures (NA = 1.0, 0.7, and 0.5) were carried out. The FWHM of Gaussian focus (fg) and photonic nanojet (fp) for different incident wavelengths (λ) in water ($n_1 = 1.33$) are shown in Table 1.

Both the FWHM values and the FWHM divided by the incident wavelength (λ) are shown in this table. The FWHM values are significantly affected by all the parameters n_2, NA, D, and λ. From the table, it is clear that the FWHM values of the photonic nanojets are much smaller than the corresponding Gaussian foci. It can be seen that in all cases the FWHM has decreased when n_2 is increased (1.46 to 2.2) or NA is increased (0.5 to 1.0) or λ is decreased (1064 to 532 nm). These simulations indicate that it is possible to achieve super-resolution imaging in water with the aid of microspheres. The symbol "X" in the table indicates that a nanojet was not observed in these cases. A few representative fluence maps from COMSOL simulations are shown in Fig. 2. For a better view, a $10 \times 15\ \mu m^2$ area around the Gaussian foci/photonic nanojet is shown here. Figure 2(g) shows the normalized line profiles along with the FWHM values. The fluence maps generated for Gaussian foci and photonic nanojets were then used for k-wave simulation in MATLAB for the ORPAM light excitation source.

3.2 *Optical Resolution Photoacoustic Microscopic B-Scan Imaging with Photonic Nanojet in k-Wave*

First, the line target numerical phantom with a 20-nm width and 1000-nm length was scanned. Figures 3(a) and 3(b) show the 2-D B-scan PAM images of the line target excited with a normal Gaussian focused beam with FWHM 1164 nm [Fig. 2(e)] and excited with a photonic nanojet with FWHM 305 nm [Fig. 2(f)], respectively. It is evident that the lateral resolution has improved with the photonic nanojet excitation. Figure 3(c) shows the normalized lateral line profiles along the lines indicated on Figs. 3(a) and 3(b). From the line profiles, the lateral resolution of the ORPAM system was quantified to be 1135 and 355 nm, respectively (very close to the values measured in COMSOL from the excitation beam profiles). The slight difference is due to the grid size (20 nm) and the nonideal line target (line width 20 nm) used in the k-wave simulation.

The second numerical phantom where two square targets with side lengths 1 μm and seperated by a distance $d = 0.5\ \mu$m were imaged next. Figure 4(a) shows the ORPAM B-scan image of the targets obtained by exciting with normal the Gaussian-focused beam [Fig. 2(e)]. The targets were not resolved in this case beacuse of the poor lateral resolution (the optical spot size is larger than the speration beteen the targets). Whereas in Fig. 4(b) the targets were clearly resolved when ORPAM B-scan images were generated with photonic nanojet excitation [Fig. 2(f)]. Figure 4(c) shows the normalized line scan profiles along the lines indicated on Figs. 4(a) and 4(b). Once again, the line profiles in Fig. 4(c) confirmed the resolving ability of a separation of a 500-nm gap with the photonic nanojet excited ORPAM.

Next, similar exercises were repeated with a smaller gap of 200 nm between the two square target objects to determine the smallest gap the ORPAM system will be able to resolve. The excitation light source used was the smallest photonic nanojet that was simulated with the set of parameters in this study [FWHM 208 nm Fig. 2(b)]. Figure 5(a) shows the ORPAM B-scan image and Fig. 5(b) shows the normalized profile along the line indicated on Fig. 5(a). The targets are resolved in this case as expected, demonstrating the ability of breaking through the diffraction-limited lateral resolution in ORPAM with the help of photonic nanojets to achieve super-resolution.

The super-resolution ORPAM modality presented in this work promises to enhance the lateral resolution beyond the diffraction limit. This approach may revolutionize the fundamental biological studies involving cellular structures, vasculature, and microcirculation systems. Melanoma arises from deadly skin cancer melanocytes, and so on.[16,38] Currently, the diagnosis

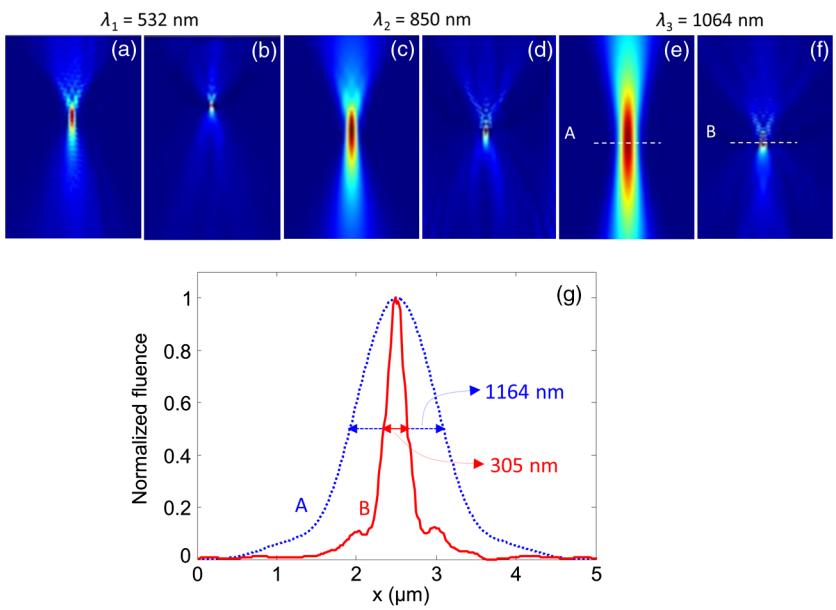

Fig. 2 Numerical simulation of Gaussian foci and photonic nanojets using FEM in COMSOL: Gaussian beam foci for (a) $\lambda_1 = 532$ nm, $D = 5\ \mu$m, NA $= 1.0$, (c) $\lambda_2 = 850$ nm, $D = 10\ \mu$m, NA $= 0.7$, (e) $\lambda_3 = 1064$ nm, $D = 15\ \mu$m, NA $= 0.5$, photonic nanojets for (b) $\lambda_1 = 532$ nm, $D = 5\ \mu$m, NA $= 1.0$, $n_2 = 1.6$, (d) $\lambda_2 = 850$ nm, $D = 10\ \mu$m, NA $= 0.7$, $n_2 = 2.2$, (f) $\lambda_3 = 1064$ nm, $D = 15\ \mu$m, NA $= 0.5$, $n_2 = 2.2$. (g) Normalized line scan profiles along the lines A and B indicated on Figs. 2(e) and 2(f), respectively. COMSOL simulations were carried out in 30×60-μm^2 area, however, 10×15-μm^2 area around the focus is shown here.

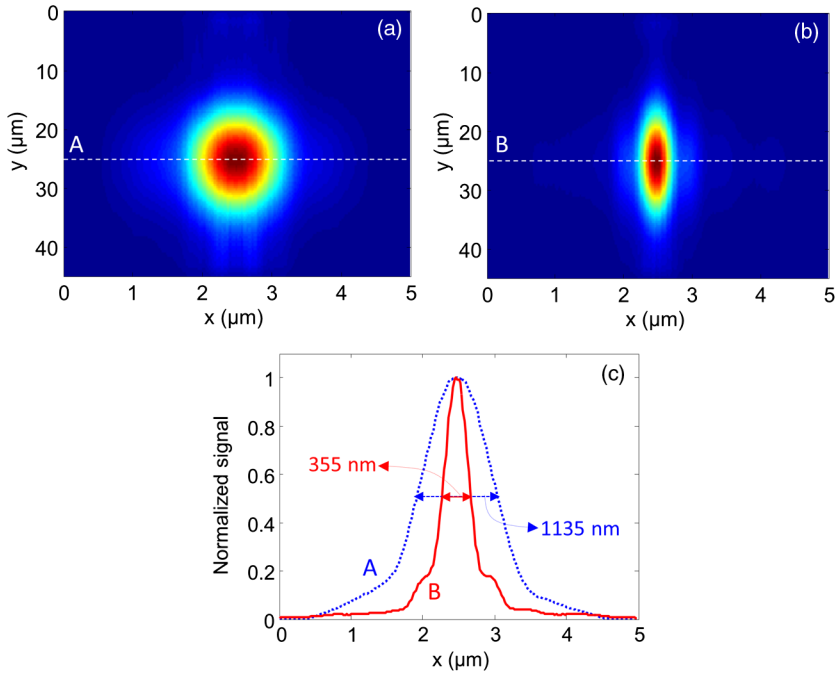

Fig. 3 k-wave simulation of B-scan PAM image with a line absorber target object [20-nm line width, length 1000 nm]. B-scan image obtained with (a) Gaussian focus light [shown in Fig. 2(e)] excitation, (b) photonic nanojet [shown in Fig. 2(f)] excitation. (c) Normalized line scan profiles (point spread function) along the dotted lines A and B indicated on 3(a) and 3(b), respectively.

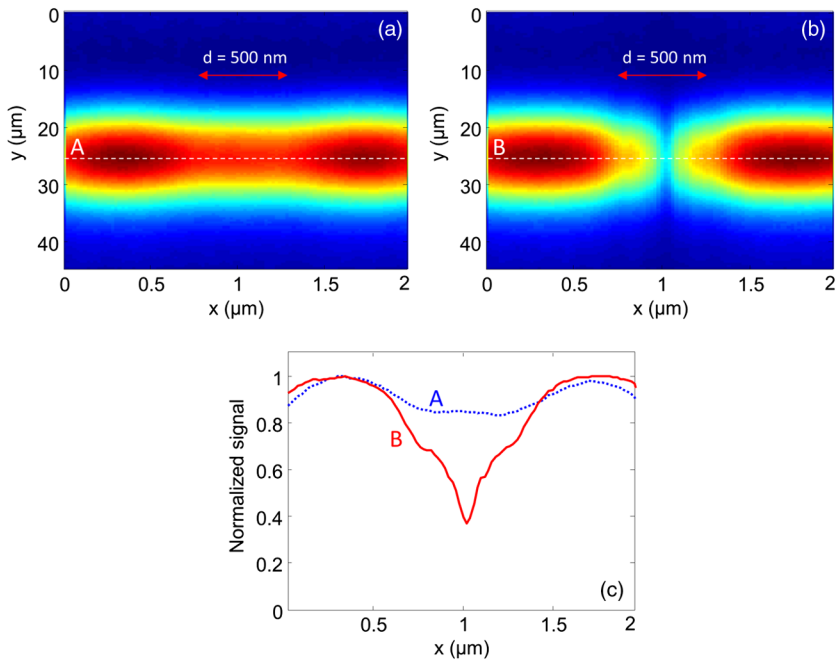

Fig. 4 k-wave simulation of PAM B-scan images of two square (size 1 μm) targets separated by a gap of 500 nm. B-scan image with (a) Gaussian focus [shown in Fig. 2(e)] excitation, (b) photonic nanojet [shown in Fig. 2(f)] excitation. (c) Normalized line scan profiles along the dotted lines A and B indicated on 4(a) and 4(b), respectively.

of melanoma is done based on invasive biopsy and inaccurate visual inspection. Super-resolution ORPAM (being an *in vivo*, label-free, noninvasive technique) will help us to diagnose melanoma in the early stages, a key to successful treatment. Tumor angiogenesis, a hallmark of cancer, is presently imaged either *in vivo* by clinical methods at low resolution or *ex vivo* by nonclinical methods at high resolution.[16,39] Super-resolution ORPAM, having high endogenous contrast, can image angiogenic microvessels *in vivo*. However, the drawback with this approach is limited penetration depth compared to the conventional ORPAM. The generated nanojets are limited in depth, as observed from the simulations. One can play with various

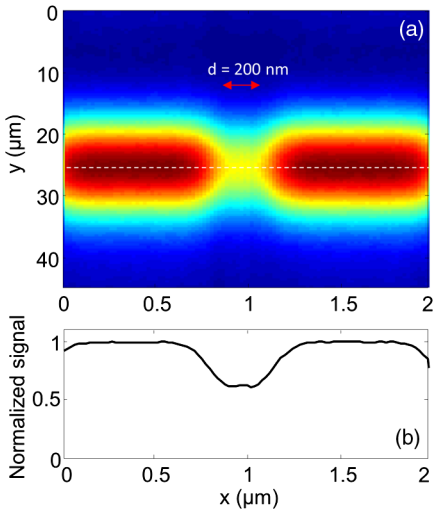

Fig. 5 k-wave simulation of PAM B-scan images of two square (size 1 μm) targets separated by a gap of 200 nm. (a) B-scan image with photonic nanojet [shown in Fig. 2(d)] excitation. (b) Normalized line scan profile along the dotted line indicated on (a).

parameters such as the diameter of the microsphere, the refractive-index of the material of the microsphere, etc., to move the focusing spot (nanojets) at various depths from the surface of the microsphere. We can also use some form of z-scanning to increase the depth of imaging. We may not reach the depth penetration of conventional ORPAM, however, it can be significantly improved. In the future, we will work on experimentally implementing the super-resolution ORPAM and applying it to cellular imaging. Improving the penetration depth of super-resolution ORPAM will also be a challenging task to overcome in the future.

4 Conclusions

In this work, through numerical simulations it has been demonstrated that it is possible to achieve super-resolution in optical resolution PAM using microspheres. The formation of the Gaussian foci and photonic nanojets in a water medium were studied for various parameters of the light focusing objective, microsphere refractive index, size, and excitation wavelengths. For a given NA, by proper selection of the incident wavelength and microsphere refractive index more than twofold lateral resolution improvement is achievable in conventional ORPAM. In our simulations, ~fourfold improvement in lateral resolution was observed with 0.5 NA, 1064 nm, $n_2 = 2.2$, $D = 15$ μm. This method is simple, cost effective, and can provide far-field super-resolution which allows flexibility of the system for *in vivo* imaging. This approach opens new opportunities for many biomedical imaging applications, such as cellular, subcellular, microcirculation systems, and tumor angiogenesis that require higher lateral resolution than that obtained at present. In the future, we will experimentally implement the photonic nanojet approach to achieve super-resolution in ORPAM.

Acknowledgments

The work was funded by the University Start-up Grant at Nanyang Technological University, National Natural Science Foundation of China (Grant No. 61301053), and the Fundamental Research Funds for the Central Universities.

References

1. X. D. Wang et al., "Noninvasive laser-induced photoacoustic tomography for structural and functional *in vivo* imaging of the brain," *Nat. Biotechnol.* **21**(7), 803–806 (2003).
2. S. A. Ermilov et al., "Laser optoacoustic imaging system for detection of breast cancer," *J. Biomed. Opt.* **14**(2), 024007 (2009).
3. L. V. Wang and S. Hu, "Photoacoustic tomography: *in vivo* imaging from organelles to organs," *Science* **335**(6075), 1458–1462 (2012).
4. X. D. Wang et al., "Three-dimensional laser-induced photoacoustic tomography of mouse brain with the skin and skull intact," *Opt. Lett.* **28**(19), 1739–1741 (2003).
5. X. Yang and L. V. Wang, "Monkey brain cortex imaging by photoacoustic tomography," *J. Biomed. Opt.* **13**(4), 044009 (2008).
6. M. Pramanik et al., "Design and evaluation of a novel breast cancer detection system combining both thermoacoustic (TA) and photoacoustic (PA) tomography," *Med. Phys.* **35**(6), 2218 (2008).
7. W. Xia et al., "Design and evaluation of a laboratory prototype system for 3D photoacoustic full breast tomography," *Biomed. Opt. Express* **4**(11), 2555–2569 (2013).
8. Y. Xu, M. H. Xu, and L. V. Wang, "Exact frequency-domain reconstruction for thermoacoustic tomography—II: cylindrical geometry," *IEEE Trans. Med. Imaging* **21**(7), 829–833 (2002).
9. G. Paltauf et al., "Iterative reconstruction algorithm for optoacoustic imaging," *J. Acoust. Soc. Am.* **112**(4), 1536 (2002).
10. B. T. Cox et al., "Two-dimensional quantitative photoacoustic image reconstruction of absorption distributions in scattering media by use of a simple iterative method," *Appl. Opt.* **45**(8), 1866–1875 (2006).
11. K. Wang et al., "Investigation of iterative image reconstruction in three-dimensional optoacoustic tomography," *Phys. Med. Biol.* **57**(17), 5399–5423 (2012).
12. J. Prakash et al., "Basis pursuit deconvolution for improving model-based reconstructed images in photoacoustic tomography," *Biomed. Opt. Express* **5**(5), 1363 (2014).
13. J. Yao and L. V. Wang, "Sensitivity of photoacoustic microscopy," *Photoacoustics* **2**(2), 87–101 (2014).
14. K. Maslov, G. Stoica, and L. V. Wang, "*In vivo* dark-field reflection-mode photoacoustic microscopy," *Opt. Lett.* **30**(6), 625–627 (2005).
15. H. F. Zhang et al., "Functional photoacoustic microscopy for high-resolution and noninvasive *in vivo* imaging," *Nat. Biotechnol.* **24**(7), 848–851 (2006).
16. C. Zhang, K. Maslov, and L. V. Wang, "Subwavelength-resolution label-free photoacoustic microscopy of optical absorption *in vivo*," *Opt. Lett.* **35**(19), 3195–3197 (2010).
17. S. Hu, K. Maslov, and L. V. Wang, "Second-generation optical-resolution photoacoustic microscopy with improved sensitivity and speed," *Opt. Lett.* **36**(7), 1134–1136 (2011).
18. G. Li, K. I. Maslov, and L. V. Wang, "Reflection-mode multifocal optical-resolution photoacoustic microscopy," *J. Biomed. Opt.* **18**(3), 030501 (2013).
19. W. Xing et al., "Integrated optical- and acoustic-resolution photoacoustic microscopy based on an optical fiber bundle," *Opt. Lett.* **38**(1), 52–54 (2013).
20. W. Shi et al., "*In vivo* dynamic process imaging using real-time optical-resolution photoacoustic microscopy," *J. Biomed. Opt.* **18**(2), 026001 (2013).
21. M. Xu and L. V. Wang, "Analytic explanation of spatial resolution related to bandwidth and detector aperture size in thermoacoustic or photoacoustic reconstruction," *Phys. Rev. E* **67**(5), 056605 (2003).
22. M. Haltmeier and G. Zangerl, "Spatial resolution in photoacoustic tomography: effects of detector size and detector bandwidth," *Inverse Probl.* **26**(12), 125002 (2010).
23. K. Maslov et al., "Optical-resolution photoacoustic microscopy for *in vivo* imaging of single capillaries," *Opt. Lett.* **33**(9), 929–931 (2008).
24. L. V. Wang, "Tutorial on photoacoustic microscopy and computed tomography," *IEEE J. Sel. Top. Quantum Electron.* **14**(1), 171–179 (2008).
25. A. Heifetz et al., "Photonic Nanojets," *J. Comput. Theoritical Nanosci.* **6**(9), 1979–1992 (2009).
26. Z. Wang et al., "Optical virtual imaging at 50 nm lateral resolution with a white-light nanoscope," *Nat. Commun.* **2**, 218 (2011).
27. X. Hao et al., "Microsphere based microscope with optical super-resolution capability," *Appl. Phys. Lett.* **99**(20), 203102 (2011).

28. A. Darafsheh et al., "Optical super-resolution by high-index liquid-immersed microspheres," *Appl. Phys. Lett.* **101**(14), 141128 (2012).
29. L. Li et al., "Label-free super-resolution imaging of adenoviruses by submerged microsphere optical nanoscopy," *Light: Sci. Appl.* **2**(9), e104 (2013).
30. H. Yang et al., "Super-resolution biological microscopy using virtual imaging by a microsphere nanoscope," *Small* **10**(9), 1712–1718 (2014).
31. J. Kasim et al., "Near-field Raman imaging using optically trapped dielectric microsphere," *Opt. Express* **16**(11), 7976–7984 (2008).
32. P. K. Upputuri et al., "Super-resolution coherent anti-Stokes Raman scattering microscopy with photonic nanojets," *Opt. Express* **22**(11), 12890–12899 (2014).
33. J. Yao et al., "Photoimprint photoacoustic microscopy for three-dimensional label-free subdiffraction imaging," *Phys. Rev. Lett.* **112**(1), 014302 (2014).
34. J. Chen et al., "Blind-deconvolution optical-resolution photoacoustic microscopy *in vivo*," *Opt. Express* **21**(6), 7316–7327 (2013).
35. B. E. Treeby and B. T. Cox, "k-Wave: MATLAB toolbox for the simulation and reconstruction of photoacoustic wave fields," *J. Biomed. Opt.* **15**(2), 021314 (2010).
36. B. E. Treeby, E. Z. Zhang, and B. T. Cox, "Photoacoustic tomography in absorbing acoustic media using time reversal," *Inverse Probl.* **26**(11), 115003 (2010).
37. C. Zhang et al., "*In vivo* photoacoustic microscopy with 7.6-μm axial resolution using a commercial 125-MHz ultrasonic transducer," *J. Biomed. Opt.* **17**(11), 116016 (2012).
38. V. Gray-Schopfer, C. Wellbrock, and R. Marais, "Melanoma biology and new targeted therapy," *Nature* **445**(7130), 851–857 (2007).
39. D. M. McDonald and P. L. Choyke, "Imaging of angiogenesis: from microscope to clinic," *Nat. Med.* **9**(6), 713–725 (2003).

Paul Kumar Upputuri is currently working as a research fellow at Nanyang Technological University. He received a PhD in physics from the Indian Institute of Technology (IIT), Madras, in 2010. He has published around 50 papers in journals and conference proceedings. His research areas are biomedical imaging, coherent Raman microscopy, ultrafast-lasers, optical metrology, and instrumentation. He is a member of SPIE, OSA, Indian Laser Association (ILA), and Optical Society of Indian (OSI).

Zhou-Bin Wen is a MS student at the University of Electronic Science & Technology of China. His research area is mainly in electromagnetic simulation.

Zhe Wu is an associate professor at the National Laboratory for Vacuum Electronics, School of Physical Electronics, University of Electronic Science & Technology of China. His research areas are mainly in electromagnetic simulation, optical and electrical characterization for micro/nano structures and application of microwave energy.

Manojit Pramanik is an assistant professor in the School of Chemical and Biomedical Engineering at Nanyang Technological University, Singapore. He received his PhD in biomedical engineering from Washington University in St. Louis, MO, USA. His research interests include development of photoacoustic/thermoacoustic imaging systems, image reconstruction method, breast cancer imaging, molecular imaging, contrast agent development, and Monte Carlo simulation of light propagation in biological tissue.